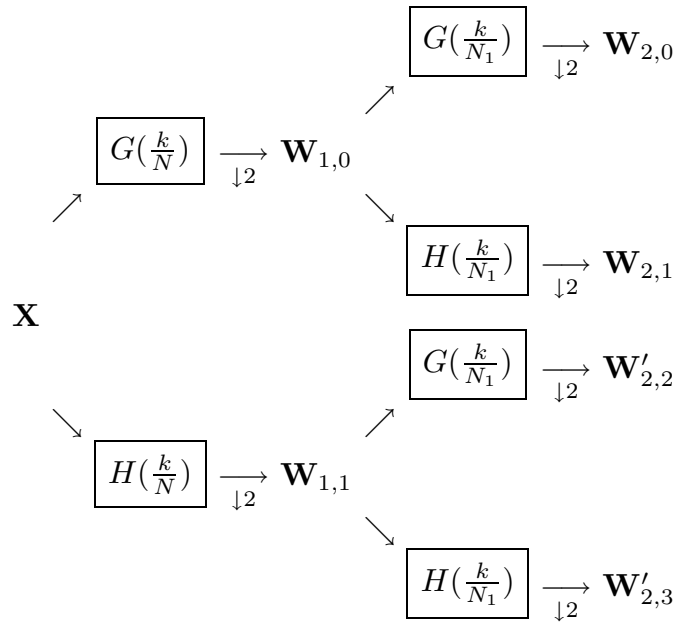
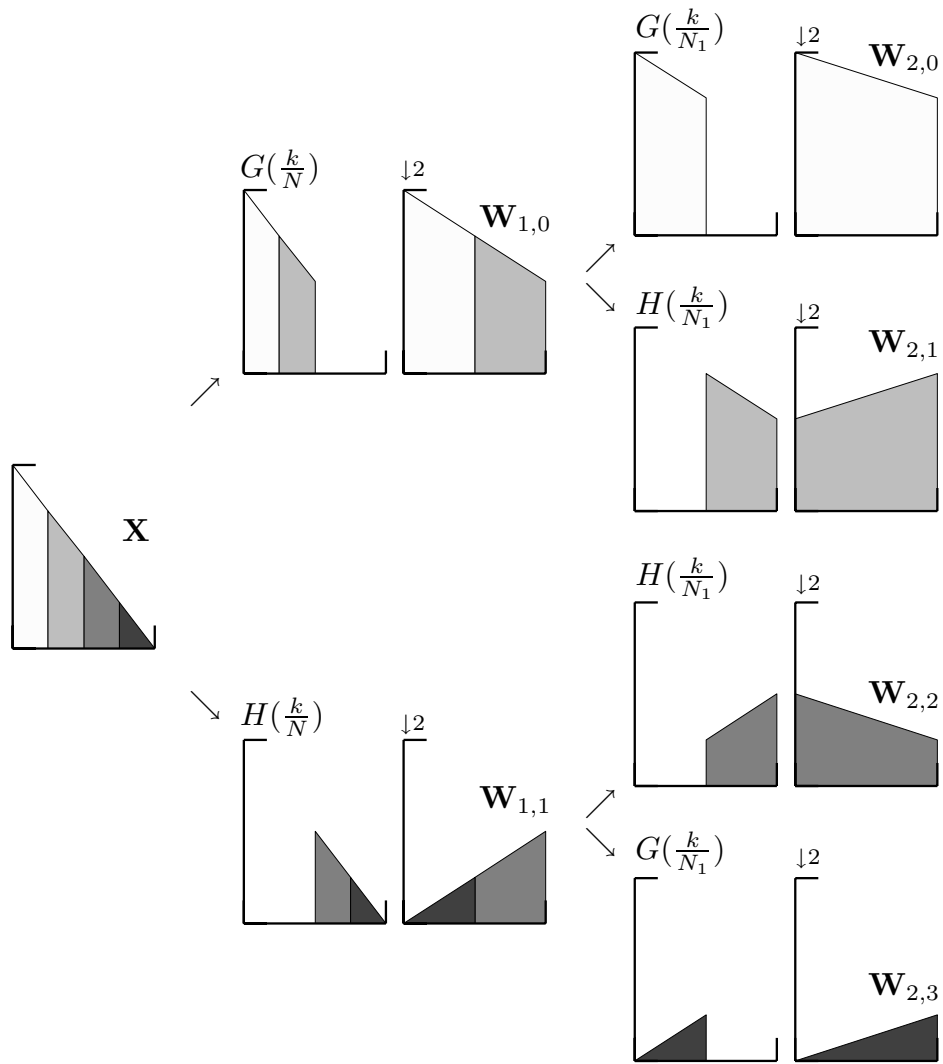


**Figure 210a.** Flow diagram illustrating the analysis of  $\mathbf{X}$  into  $\mathbf{W}_{2,0}$ ,  $\mathbf{W}_{2,1}$ ,  $\mathbf{W}_{2,2}$  and  $\mathbf{W}_{2,3}$  (sequency ordering). In the above recall that  $N_1 \equiv N/2$ .



**Figure 210b.** Flow diagram illustrating the analysis of  $\mathbf{X}$  into  $\mathbf{W}_{2,0}$ ,  $\mathbf{W}_{2,1}$ ,  $\mathbf{W}'_{2,2}$  and  $\mathbf{W}'_{2,3}$  (natural ordering).



**Figure 211.** Illustration of effect in the frequency domain of filtering with ideal low- and high-pass filters  $G(\cdot)$  and  $H(\cdot)$ , followed by downsampling (this figure parallels the flow diagram in Figure 210a). The magnitude squared DFT for the input  $\mathbf{X}$  of length  $N$  is assumed to roll off linearly as  $f$  sweeps from 0 up to the Nyquist frequency. Filtering  $\mathbf{X}$  with either  $G(\cdot)$  or  $H(\cdot)$  yields a half-band series that, after downsampling, becomes a full-band series (either  $\mathbf{W}_{1,0}$  or  $\mathbf{W}_{1,1}$ , each with  $N/2$  points). A second round of filtering and downsampling yields four new full-band series, namely,  $\mathbf{W}_{2,n}$ ,  $n = 0, 1, 2$  and  $3$ . Each  $\mathbf{W}_{2,n}$  is of length  $N/4$  and is related to a single quarter-band in  $\mathbf{X}$ . Note that, each time that we create a half-band series by filtering with  $H(\cdot)$ , the subsequent downsampling creates a full-band series whose frequency content is reversed with respect to that of the half-band series; on the other hand, filtering with  $G(\cdot)$  causes no such reversal (for an explanation of the reversal induced by  $H(\cdot)$ , see Section 4.4).

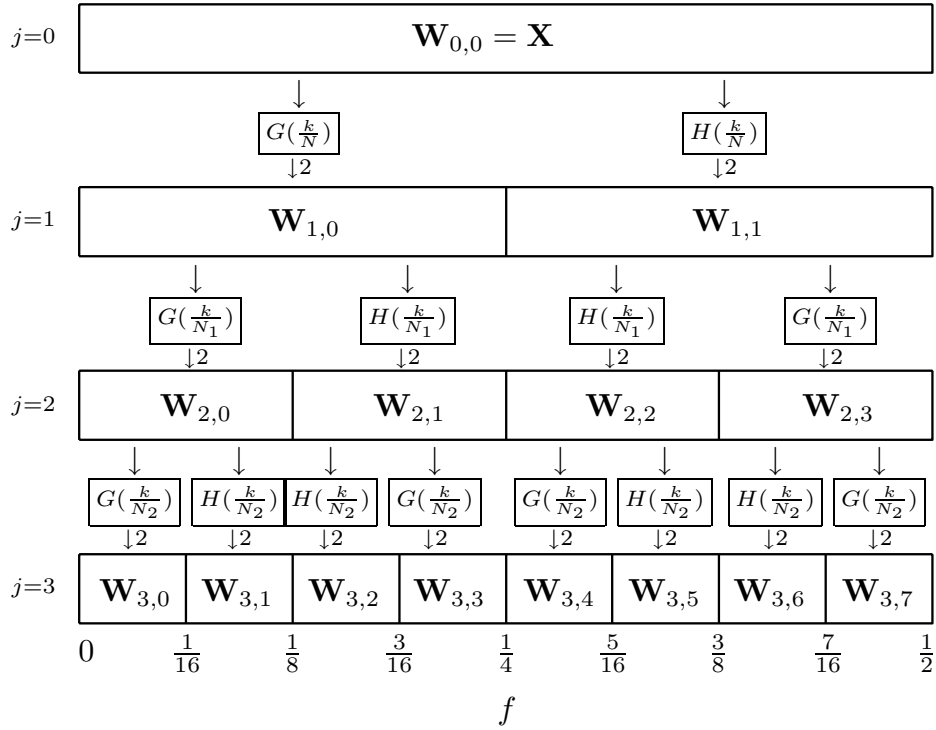


**Figure 212a.** Flow diagram illustrating the analysis of  $X$  into  $W_{3,0}, \dots, W_{3,7}$  (recall that  $N_j \equiv N/2^j$ ).

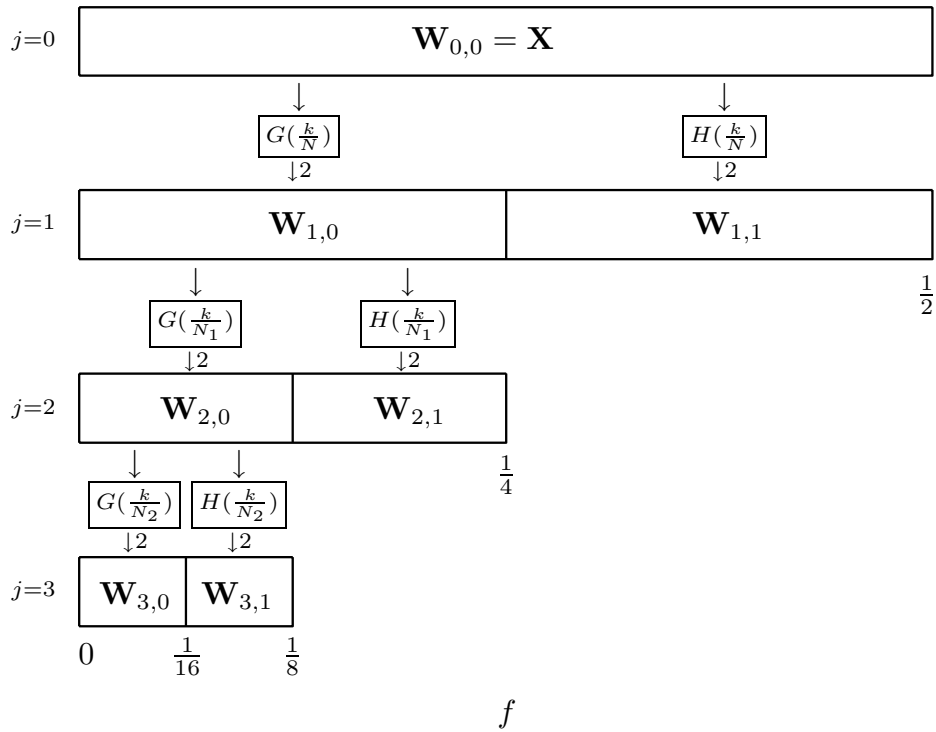


**Figure 212b.** Flow diagram illustrating the analysis of  $X$  into  $W_{3,0}, W_{3,1}, W_{2,1}$  and  $W_{1,1}$ , which is identical to a partial DWT of level  $J_0 = 3$ .

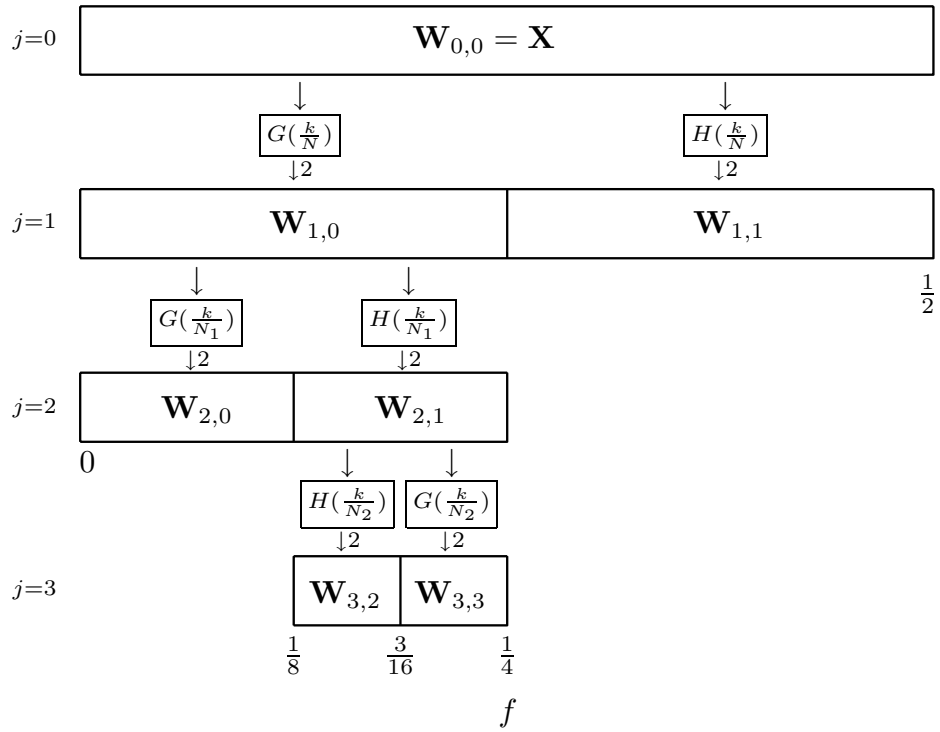


**Figure 213.** Flow diagram illustrating the analysis of  $\mathbf{X}$  into  $\mathbf{W}_{2,0}$ ,  $\mathbf{W}_{3,2}$ ,  $\mathbf{W}_{3,3}$  and  $\mathbf{W}_{1,1}$ , an arbitrary disjoint dyadic decomposition.

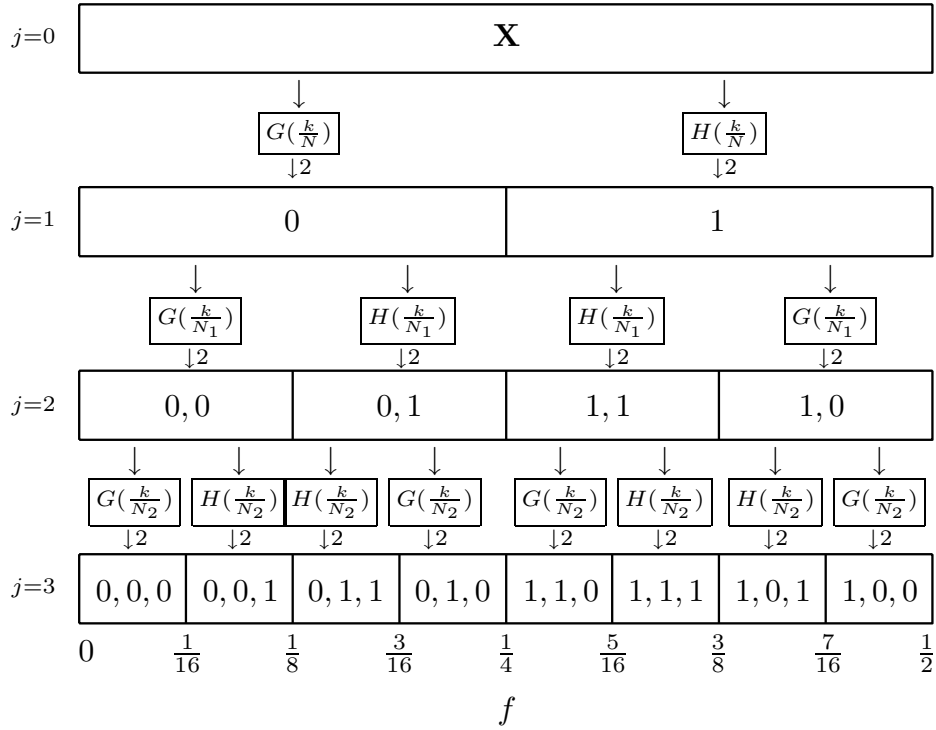


**Figure 216.** Illustration of the vectors  $\mathbf{c}_{j,n}$  for the sequency ordered WP table for levels  $j = 1, 2$  and  $3$  (0 or 1 indicate use of, respectively, a scaling (low-pass) or wavelet (high-pass) filter). Note that, if, in going from a parent node at level  $j - 1$  to a child at level  $j$ , we require use of  $G(\cdot)$ , then we append a zero to the parent's  $\mathbf{c}_{j-1, \lfloor \frac{n}{2} \rfloor}$  to obtain the child's  $\mathbf{c}_{j,n}$ ; on the other hand, if we use  $H(\cdot)$ , then we append a one. Note also that, as we sweep from left to right across either row  $j = 2$  or  $3$  and pick out the last element of each  $\mathbf{c}_{j,n}$ , we obtain the pattern '0, 1, 1, 0' or this pattern followed by a replicate (for general  $j \geq 2$ , collecting the last elements of  $\mathbf{c}_{j,n}$ ,  $n = 0, \dots, 2^j - 1$ , will yield  $2^{j-2}$  replications of '0, 1, 1, 0').

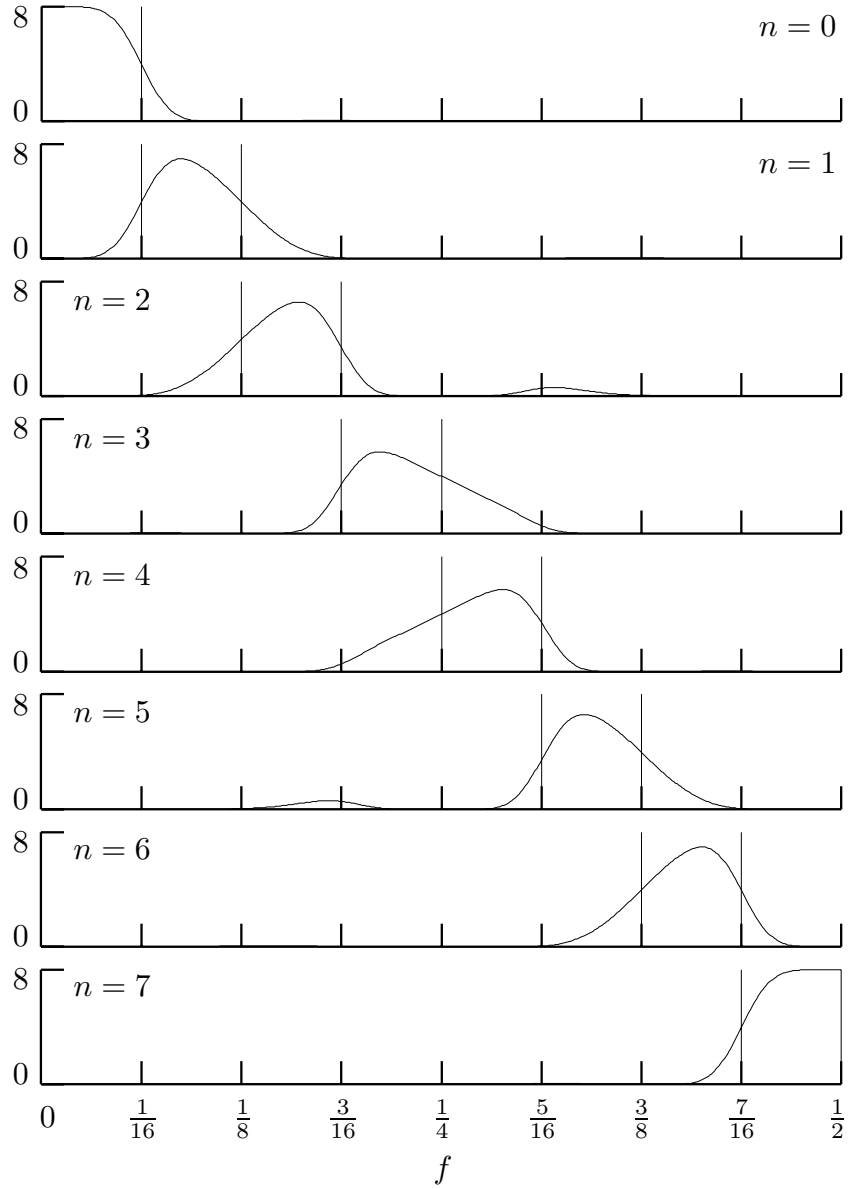


**Figure 217.** Squared gain functions  $|U_{j,n}(\cdot)|^2$  for  $j = 3$  and  $n = 0, \dots, 7$  based upon the LA(8) wavelet and scaling filters. The nominal ‘ideal’ pass-bands are marked by vertical lines.

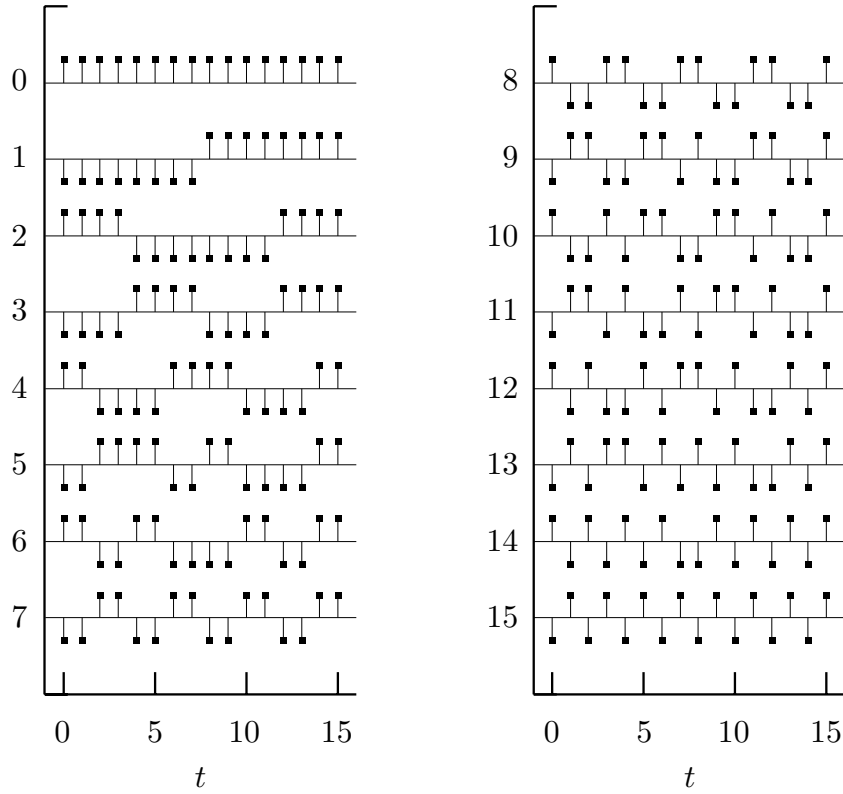


**Figure 218.** Row vectors for an  $N = 16$  DWPT of level  $J = 4$  constructed using the Haar wavelet filter. This transform is identical to what is known as the Walsh transform. The basis vectors are displayed in sequency ordering so that the inner product of (the transpose of) the  $n$ th row and a time series  $\mathbf{X}$  would yield the single element in the coefficient vector  $\mathbf{W}_{4,n}$ .

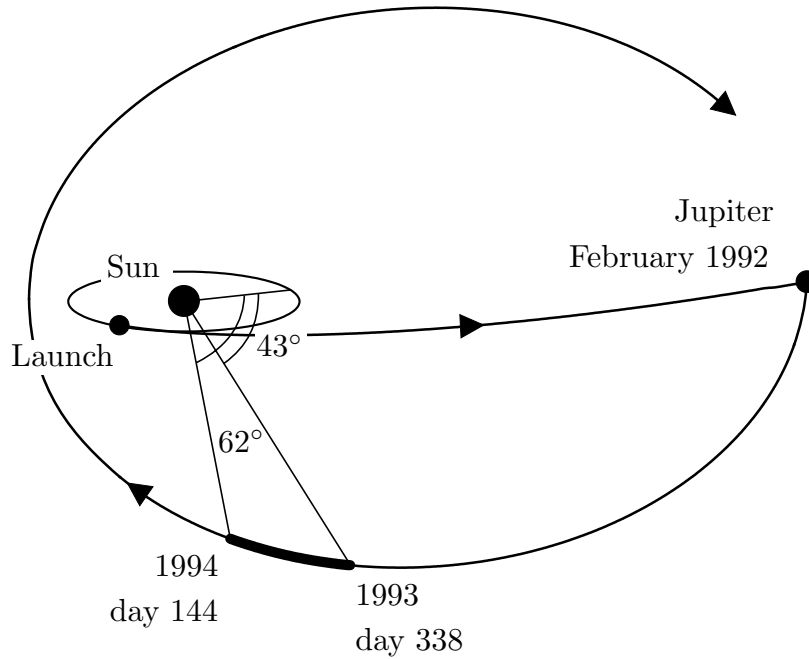


**Figure 219.** Path of the Ulysses spacecraft. After its launch, the spacecraft traveled in the plane of the Earth's orbit to near Jupiter, whose gravitational field then flung it into polar orbit about the Sun. The segment of data plotted at the bottom of Figure 222 was collected as the spacecraft traveled from heliographic latitude  $43^\circ$  S to  $62^\circ$  S south of the Sun – in changing latitudes, the spacecraft also decreased its distance from the Sun. After collecting the data of interest here, the spacecraft continued on its solar polar orbit, but now travelling north of the Sun. (Illustration courtesy of T. Horbury, Queen Mary and Westfield College, London.)



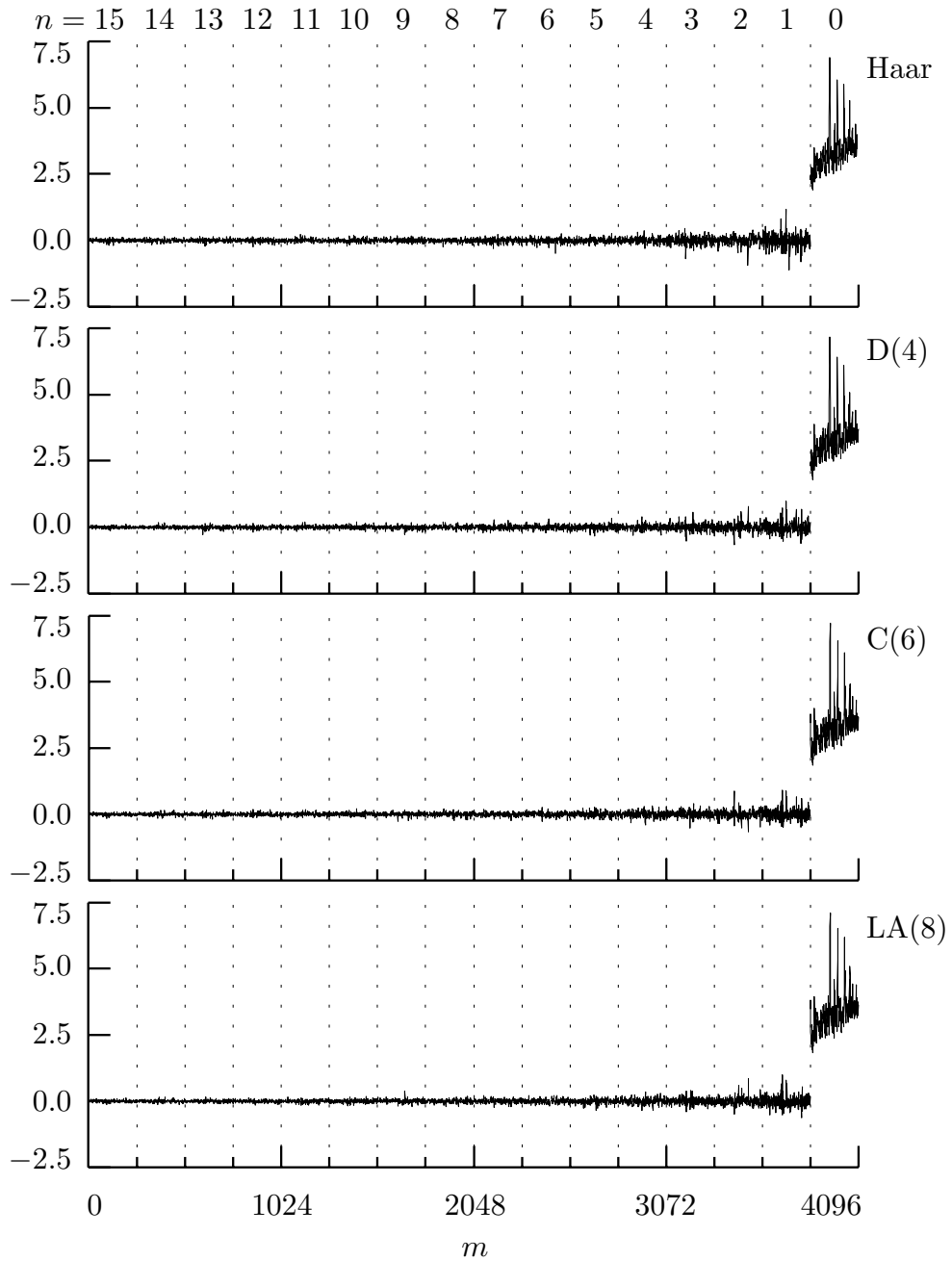


**Figure 220.** DWPT coefficients  $\mathbf{W}$  of level  $j = 4$  for solar physics time series using the Haar, D(4), C(6) and LA(8) wavelets. The elements  $W_m$  of  $\mathbf{W}$  are plotted versus  $m = 0, \dots, N-1 = 4095$ . The 15 vertical dotted lines delineate the 16 subvectors of  $\mathbf{W}$ , namely, from left to right,  $\mathbf{W}_{4,n}$ ,  $n = 15, 14, \dots, 0$ .

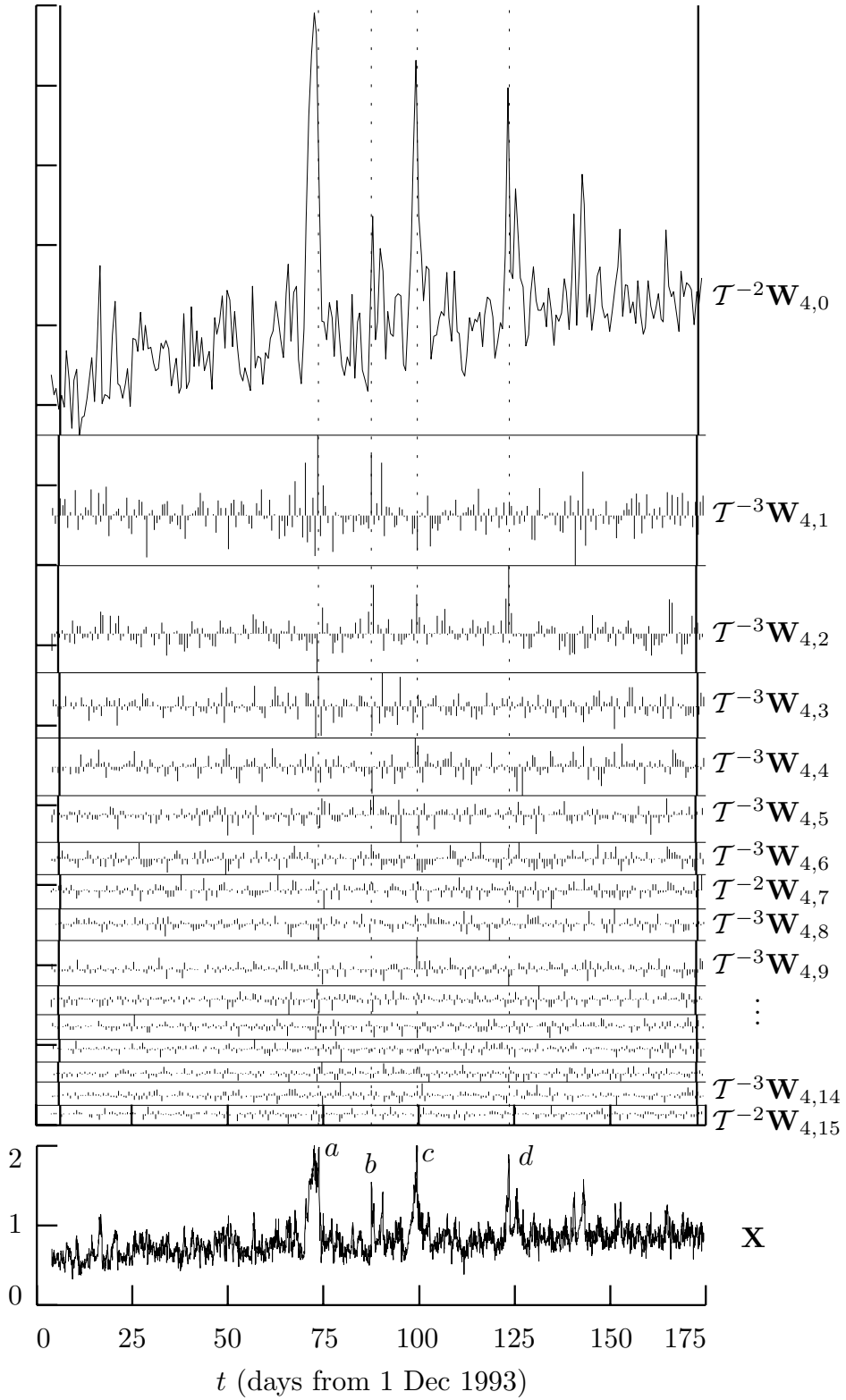


**Figure 222.** Level  $j = 4$  LA(8) DWPT coefficients for solar physics time series (see text for details).

$j=0$	$\mathbf{X}^T = [2, 0, -1, 1, 0, 0, -2, 2]$								
$j=1$	$\mathbf{W}_{1,0}^T = [\underline{\sqrt{2}}, 0, 0, 0]$				$\mathbf{W}_{1,1}^T = [-\sqrt{2}, \sqrt{2}, 0, \sqrt{8}]$				
$j=2$	$\mathbf{W}_{2,0}^T = [1, 0]$		$\mathbf{W}_{2,1}^T = [-1, 0]$		$\mathbf{W}_{2,2}^T = [2, 2]$		$\mathbf{W}_{2,3}^T = [0, \underline{2}]$		
$j=3$	$[\frac{1}{\sqrt{2}}]$	$[-\frac{1}{\sqrt{2}}]$	$[\frac{1}{\sqrt{2}}]$	$[-\frac{1}{\sqrt{2}}]$	$[\underline{\sqrt{8}}]$	$[0]$	$[\sqrt{2}]$	$[\sqrt{2}]$	
	0	$\frac{1}{16}$	$\frac{1}{8}$	$\frac{3}{16}$	$\frac{1}{4}$	$\frac{5}{16}$	$\frac{3}{8}$	$\frac{7}{16}$	$\frac{1}{2}$
	$f$								

**Figure 224.** Haar DWPT coefficients  $\mathbf{W}_{j,n}$  of levels  $j = 1, 2$  and  $3$  for a time series  $\mathbf{X}$  of length  $N = 8$ . The series  $\mathbf{X}$  was constructed from a linear combination of three basis vectors, one from each of the three levels (see Equation (224)). In the above, the DWPT coefficients corresponding to the vectors used in formation of  $\mathbf{X}$  are underlined (one each in  $\mathbf{W}_{1,0}$ ,  $\mathbf{W}_{2,3}$  and  $\mathbf{W}_{3,4}$ ).

$j=0$	1.45								
$j=1$	0.28				0.88				
$j=2$	0.19		0.19		0.72		0.36		
$j=3$	<u><b>0.12</b></u>	<u><b>0.12</b></u>	<u><b>0.12</b></u>	<u><b>0.12</b></u>	<u><b>0.32</b></u>	<u><b>0.00</b></u>	<u><b>0.28</b></u>	<u><b>0.28</b></u>	
	0	$\frac{1}{16}$	$\frac{1}{8}$	$\frac{3}{16}$	$\frac{1}{4}$	$\frac{5}{16}$	$\frac{3}{8}$	$\frac{7}{16}$	$\frac{1}{2}$
	$f$								

**Figure 225.** Cost table for the WP table shown in Figure 224. The entries in the above are the values of  $M(\mathbf{W}_{j,n})$  computed using the  $-\ell^2 \log(\ell^2)$  norm as a cost functional. The initial step of the best basis algorithm dictates that we mark the values in the bottom row in some manner – here we have done so by underlining and also by using a bold font.

$j=0$	0.96								
$j=1$	<u>0.28</u>				0.68				
$j=2$	<u>0.19</u>		<u>0.19</u>		0.32		<u>0.36</u>		
$j=3$	<u>0.12</u>	<u>0.12</u>	<u>0.12</u>	<u>0.12</u>	<u>0.32</u>	<u>0.00</u>	<u>0.28</u>	<u>0.28</u>	
	0	$\frac{1}{16}$	$\frac{1}{8}$	$\frac{3}{16}$	$\frac{1}{4}$	$\frac{5}{16}$	$\frac{3}{8}$	$\frac{7}{16}$	$\frac{1}{2}$
	$f$								

**Figure 226.** Final step of the best basis algorithm. The best basis transform is indicated by the shaded boxes. As is intuitively reasonable, the selected transform includes the three basis vectors used to form  $\mathbf{X}$ .

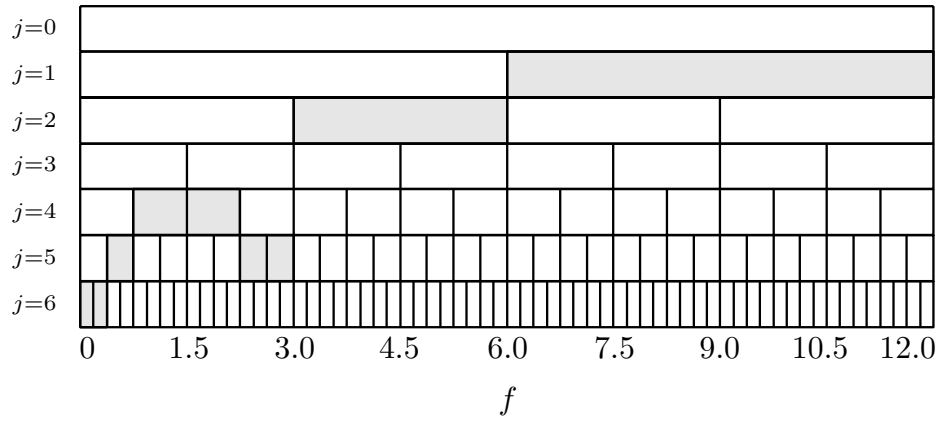


**Figure 227.** The best basis transform for the solar magnetic field magnitude data of Figure 222. This transform is based on the LA(8) wavelet filter and a cost functional based upon the  $-\ell^2 \log(\ell^2)$  norm.

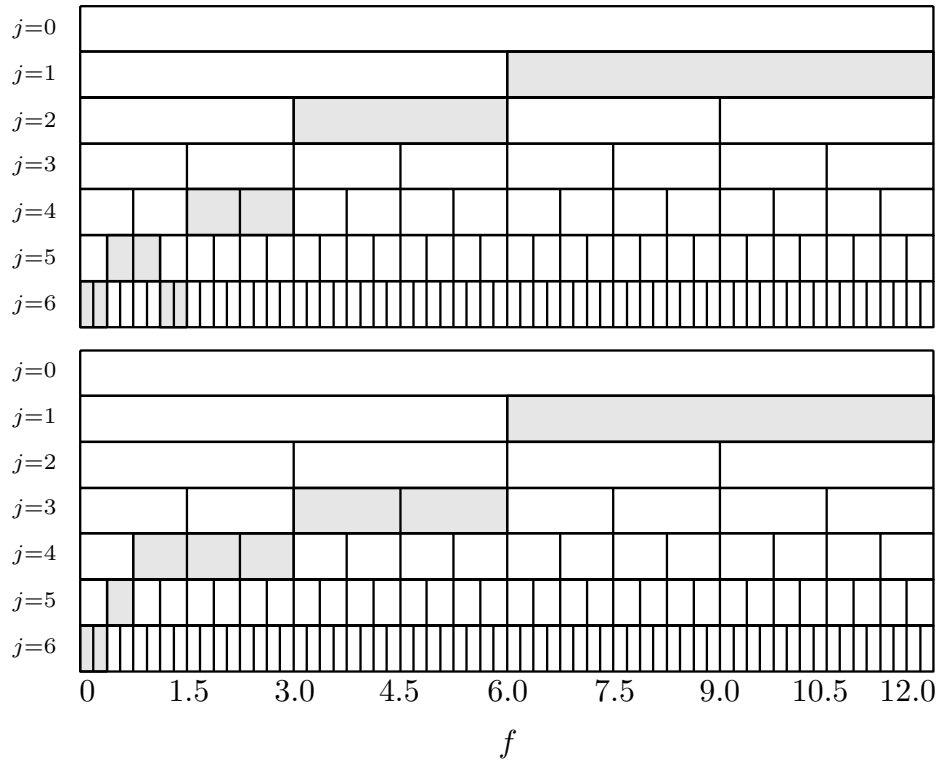


**Figure 228.** Best basis transform for the solar magnetic field magnitude data based upon reflection boundary conditions (top), and the best shift basis transform for the same data (bottom), again using reflection boundary conditions. Both transforms are based on the same wavelet filter and cost functional as used in Figure 227. The best shift basis algorithm selected the shift  $m = 52$  (i.e.,  $\mathcal{T}^{52}$ ) as the best shift.

$j$	$n$	$\mathbf{c}_{j,n}$	$S_{j,n,0}$	$S_{j,n,1}$	$ \nu_{j,n} $	LA(8)	$ p_{j,n} $	LA(8)
1	0	0	1	0	$\frac{L_1}{2} - 1$	3	$e\{g_l\}$	2.8
	1	1	0	1	$\frac{L_1}{2} + 0$	4	$e\{h_l\}$	4.2
2	0	0,0	3	0	$\frac{L_2}{2} - 2$	9	$3e\{g_l\}$	8.5
	1	0,1	1	2	$\frac{L_2}{2} + 0$	11	$e\{g_l\} + 2e\{h_l\}$	11.2
	2	1,1	0	3	$\frac{L_2}{2} + 1$	12	$3e\{h_l\}$	12.5
	3	1,0	2	1	$\frac{L_2}{2} - 1$	10	$2e\{g_l\} + e\{h_l\}$	9.8
3	0	0,0,0	7	0	$\frac{L_3}{2} - 4$	21	$7e\{g_l\}$	19.9
	1	0,0,1	3	4	$\frac{L_3}{2} + 0$	25	$3e\{g_l\} + 4e\{h_l\}$	25.2
	2	0,1,1	1	6	$\frac{L_3}{2} + 2$	27	$e\{g_l\} + 6e\{h_l\}$	27.8
	3	0,1,0	5	2	$\frac{L_3}{2} - 2$	23	$5e\{g_l\} + 2e\{h_l\}$	22.5
	4	1,1,0	4	3	$\frac{L_3}{2} - 1$	24	$4e\{g_l\} + 3e\{h_l\}$	23.8
	5	1,1,1	0	7	$\frac{L_3}{2} + 3$	28	$7e\{h_l\}$	29.1
	6	1,0,1	2	5	$\frac{L_3}{2} + 1$	26	$2e\{g_l\} + 5e\{h_l\}$	26.5
7	1,0,0	6	1	$\frac{L_3}{2} - 3$	22	$6e\{g_l\} + e\{h_l\}$	21.2	

**Table 230.** Form of the advances  $|\nu_{j,n}|$  required to achieve approximate zero phase output using a filter  $\{u_{j,n,l}\}$  based upon an LA filter with  $L/2$  even. Here we let  $j = 1, 2$  and  $3$  and  $n = 0, \dots, 2^j - 1$ . The seventh column gives specific values for the LA(8) filter (see Comments and Extensions to Section 6.5 for a discussion on the last two columns).



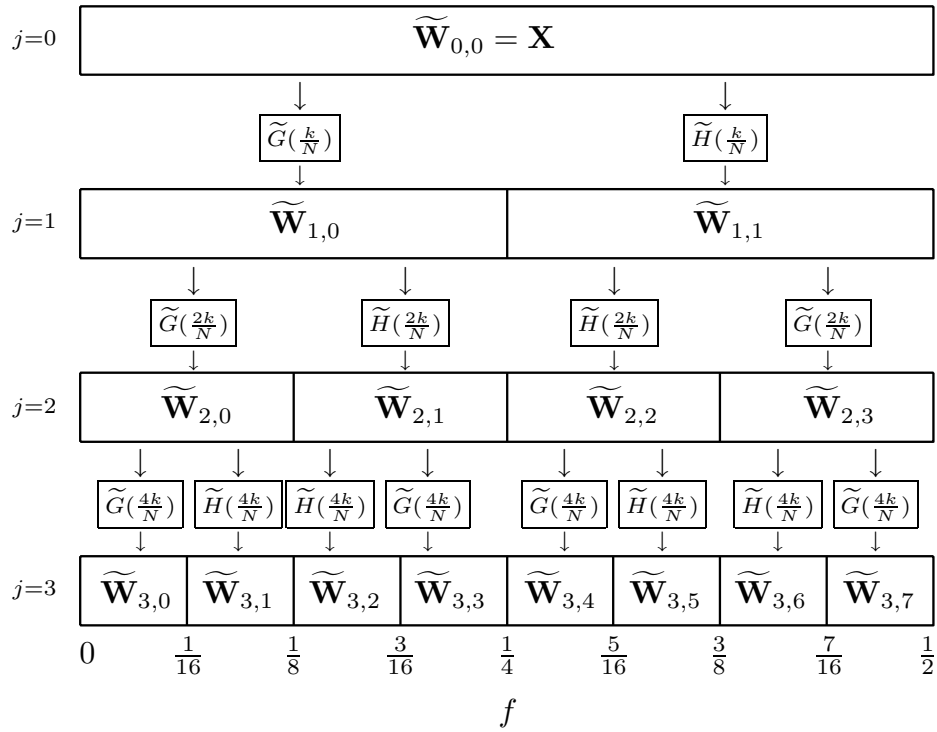


**Figure 232.** Flow diagram illustrating the analysis of  $\mathbf{X}$  into MODWPT coefficients  $\widetilde{\mathbf{W}}_{j,n}$  of levels  $j = 1, 2$  and  $3$ . Collectively, all the coefficients in the  $j$ th row constitute the level  $j$  MODWPT of  $\mathbf{X}$ . Note that, within the  $j$ th level, the frequency index  $n$  ranges from  $0$  to  $2^j - 1$  and that each  $\widetilde{\mathbf{W}}_{j,n}$  has length  $N$  (by contrast, in Figure 212a for the DWPT, each  $\mathbf{W}_{j,n}$  has length  $N/2^j$ ).

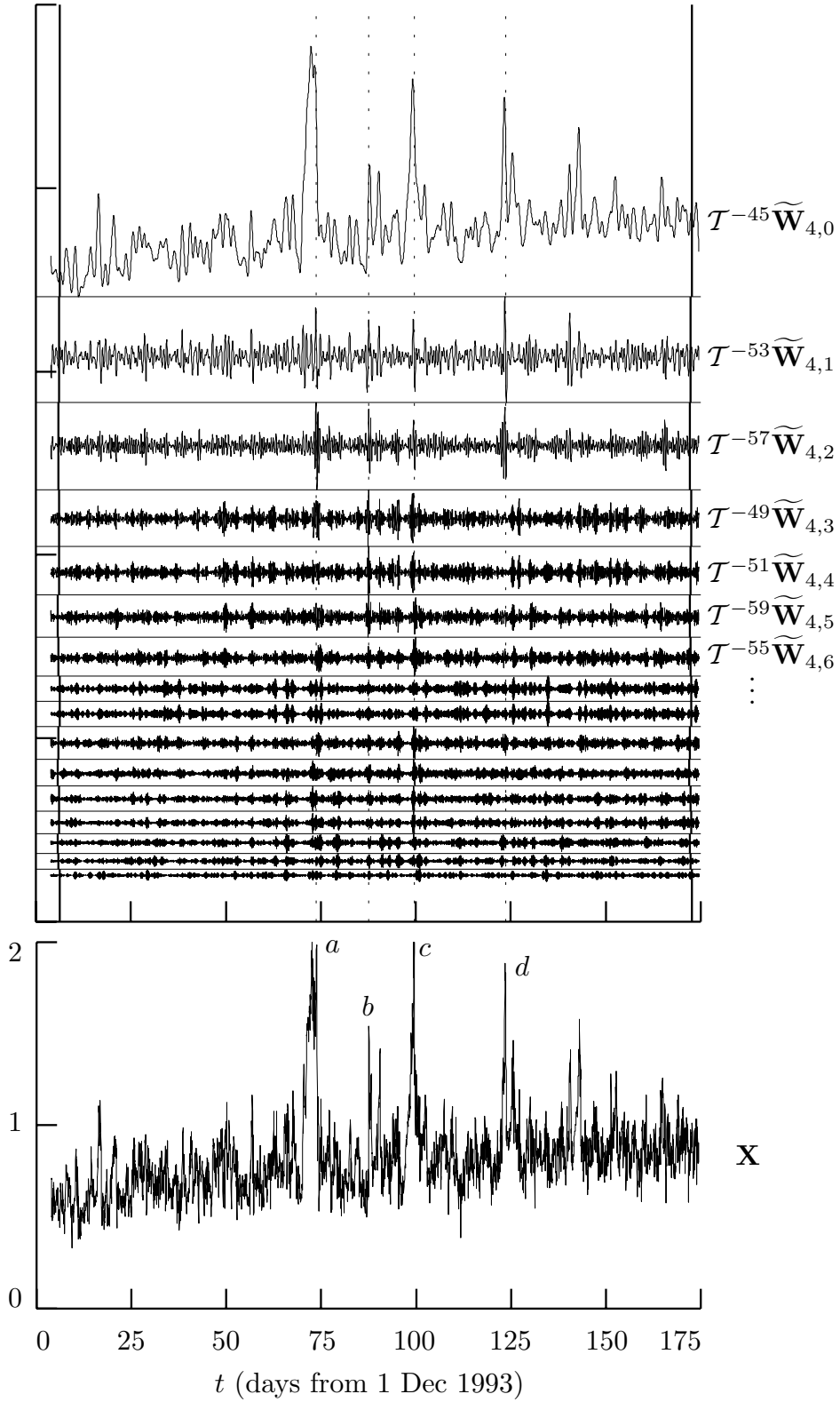


**Figure 235.** Level  $j = 4$  LA(8) MODWPT coefficients for solar physics time series (see text for details).

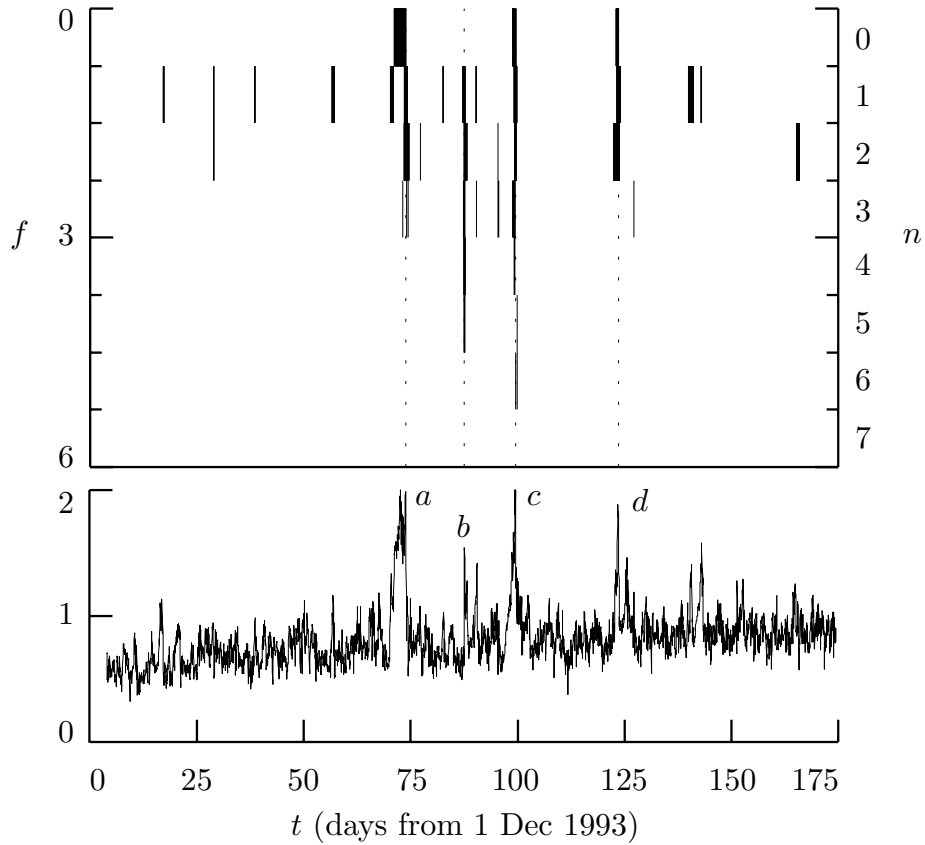


**Figure 236.** Southern hemisphere solar magnetic field magnitude data (lower plot) and corresponding modified time/frequency plot (upper). The data are measured in nanoteslas and were recorded by the Ulysses space craft from 21 hours Universal Time (UT) on day 338 of 1993 (4 December) until 12 hours UT on day 144 of 1994 (24 May). The frequency  $f$  is measured in cycles per day. The four shock wave structures are labeled  $a$  to  $d$  on the lower plot, while vertical dotted in the upper plot mark their locations as determined by Balogh *et al.* (1995).

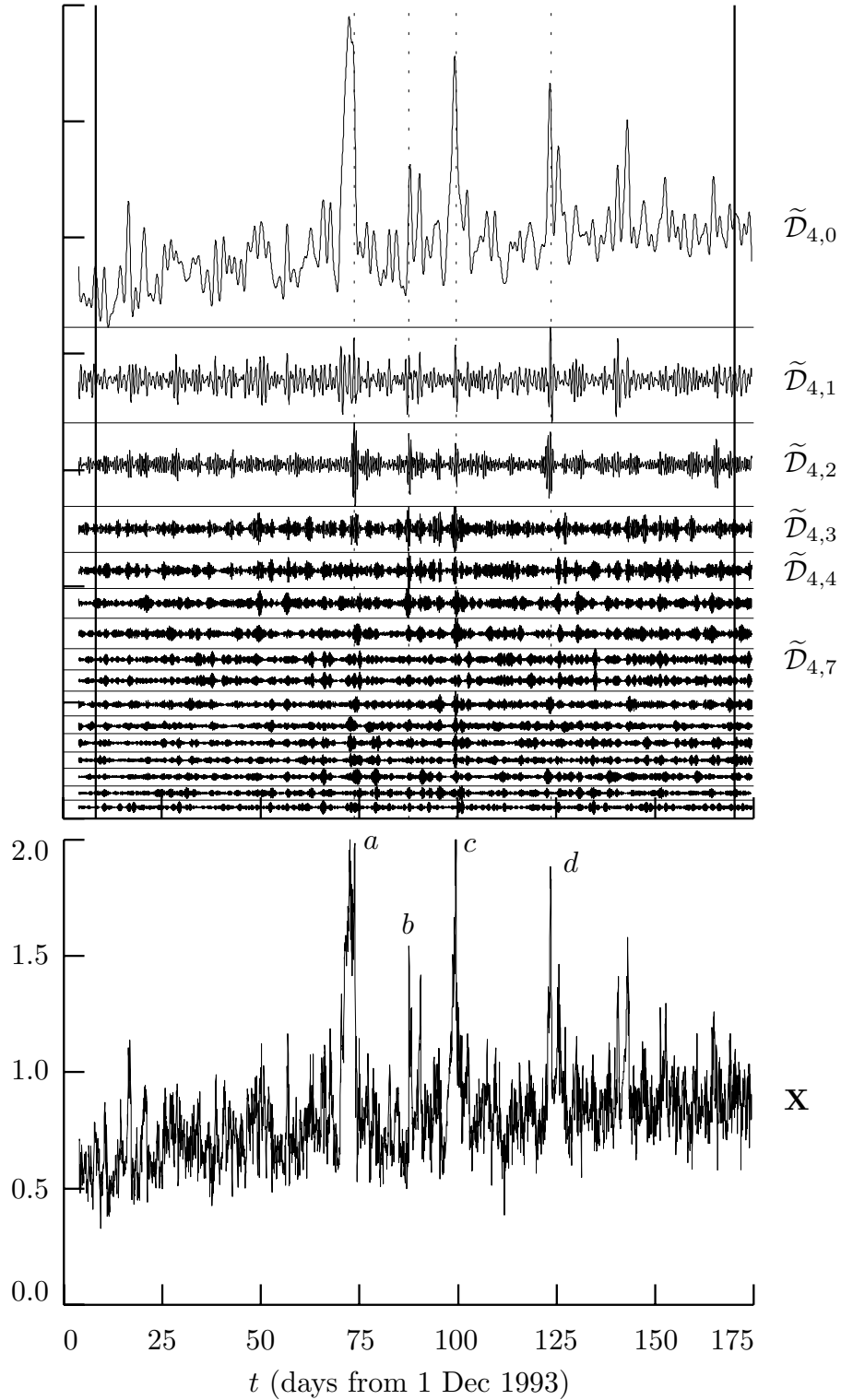


**Figure 238.** Solar magnetic field magnitude data (lower plot) and corresponding plot of the MODWPT details  $\tilde{D}_{4,n}$ ,  $n = 0, \dots, 15$  (upper). The  $n$ th detail corresponds to the frequency band from  $0.75n$  cycles per hour to  $0.75(n + 1)$  cycles per hour.

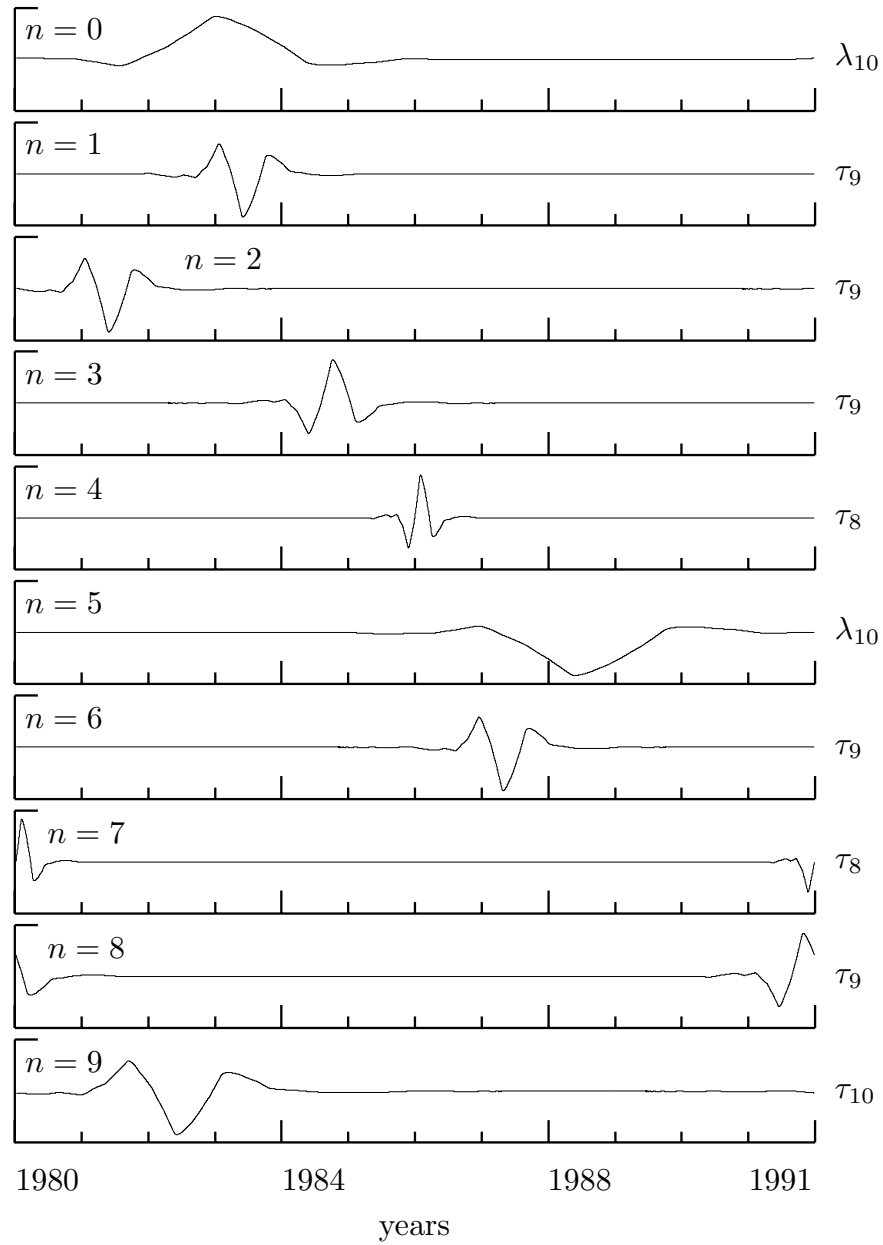


**Figure 244.** First ten MODWT vectors selected using the matching pursuit algorithm applied to the subtidal sea level fluctuations. The dictionary is  $\mathbb{D}^{(\text{modwt})}$  constructed using the LA(8) wavelet filter. Each vector has been multiplied by +1 or -1 according to the sign of its inner product with  $\mathbf{R}^{(n)}$ , thus enabling visual correlation with the original series. The standardized scale for each vector is written to the right of its plot ( $\tau_j$  for a vector from  $\tilde{\mathcal{W}}_j$  and  $\lambda_{10}$  for one from  $\tilde{\mathcal{V}}_{10}$ ).

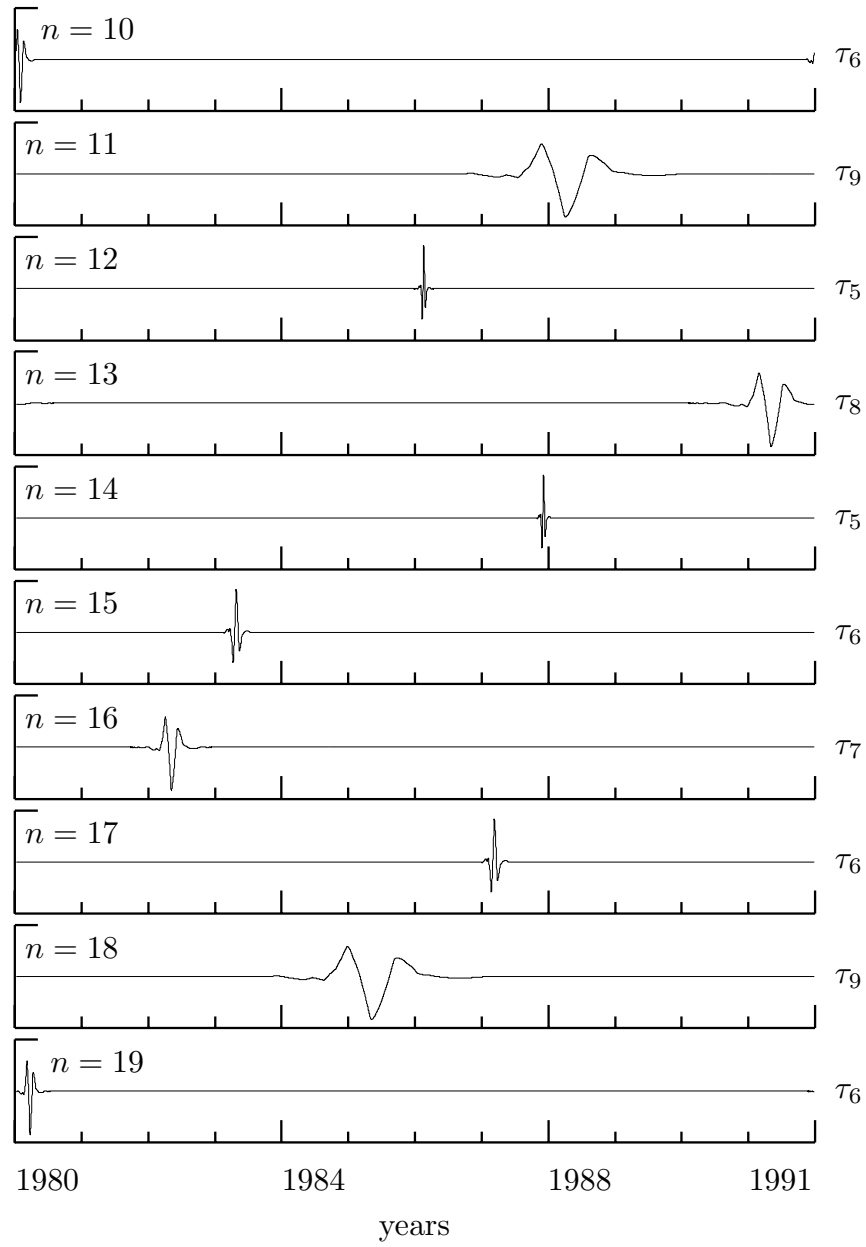


**Figure 245.** MODWT vectors selected eleventh to twentieth using the matching pursuit algorithm (see Figure 244 for details).

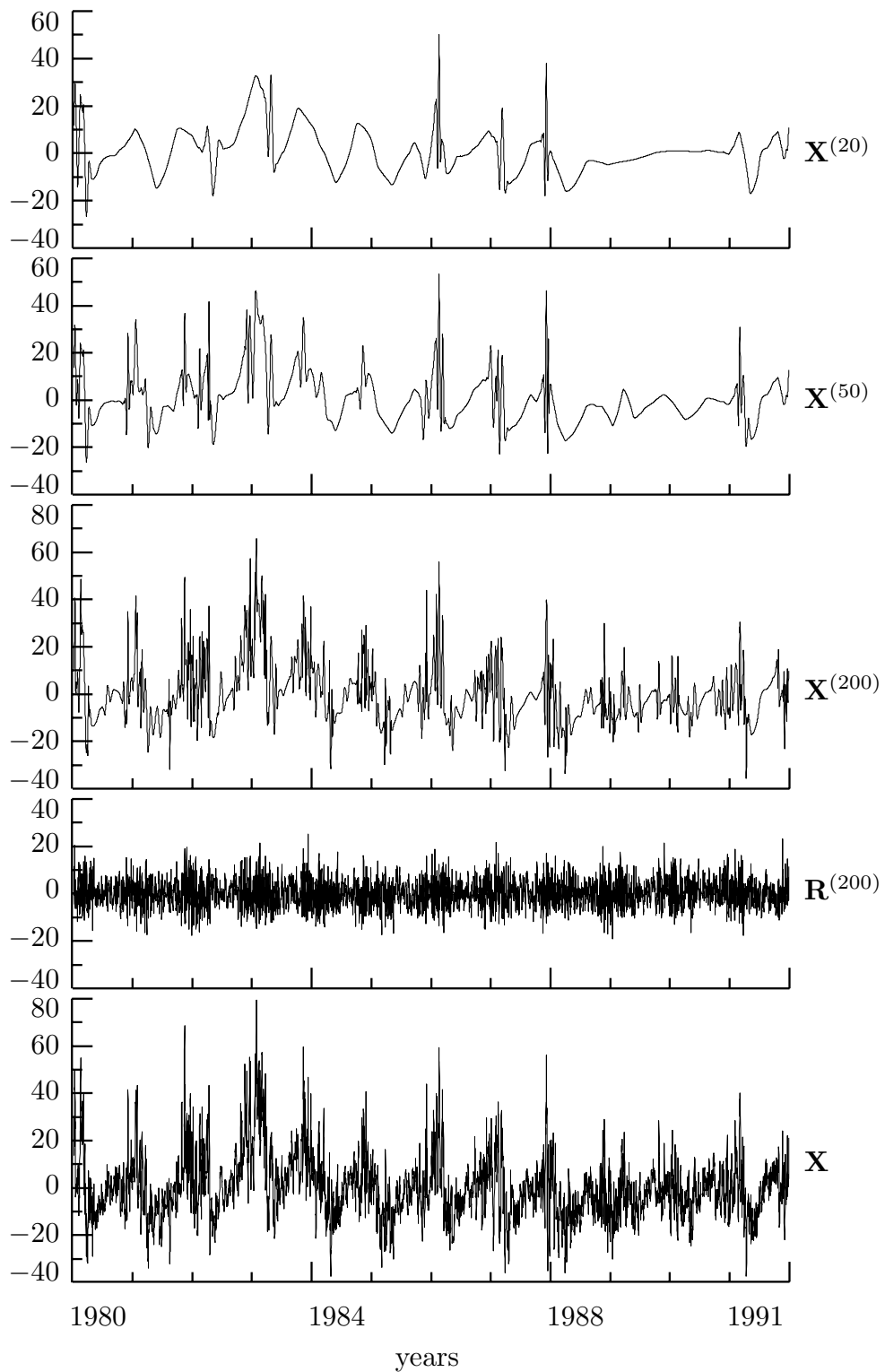


**Figure 246.** Matching pursuit approximations  $\mathbf{X}^{(m)}$  of the subtidal sea level fluctuations  $\mathbf{X}$  using  $m = 20, 50$  and  $200$  vectors from a MODWT dictionary. The residuals  $\mathbf{R}^{(200)}$  corresponding to  $\mathbf{X}^{(200)}$  are shown above the plot of  $\mathbf{X}$ .

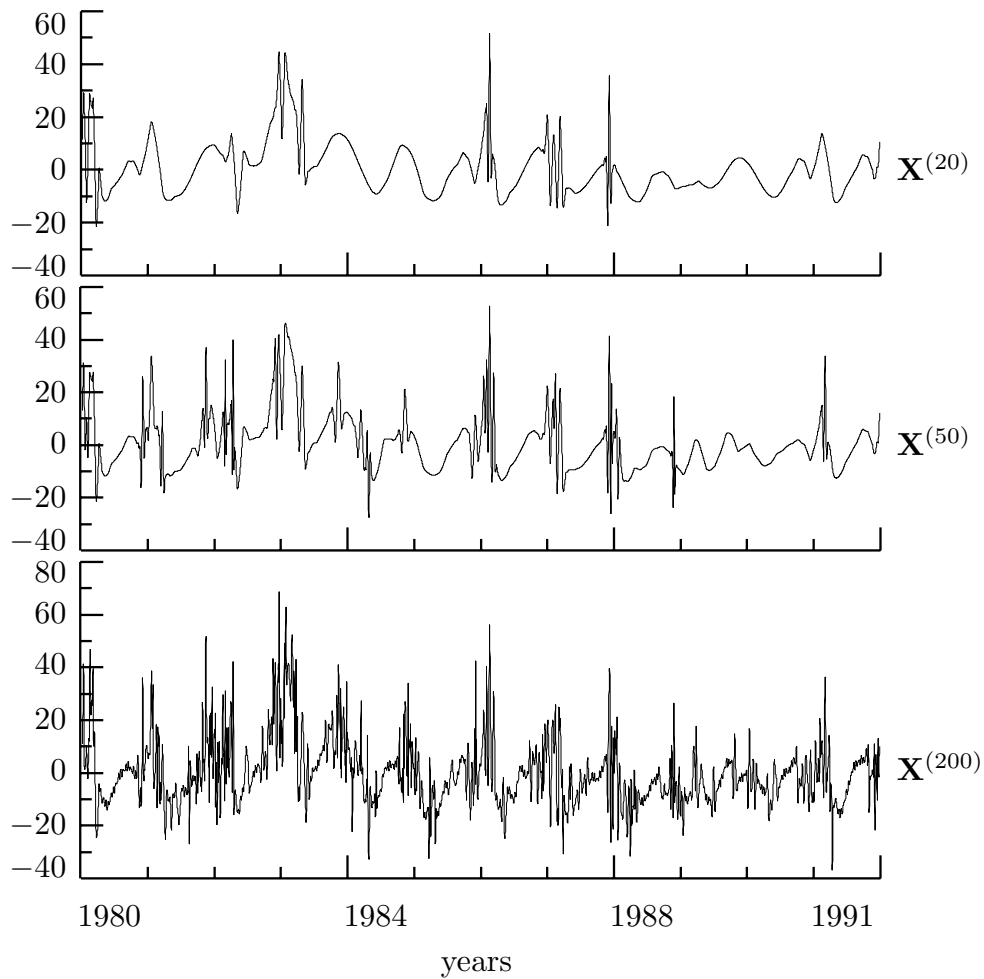


**Figure 248a.** Matching pursuit approximations  $\mathbf{X}^{(m)}$  of the subtidal sea level fluctuations  $\mathbf{X}$  using  $m = 20, 50$  and  $200$  vectors, but now from a dictionary composed of both MODWT and ODFT vectors.

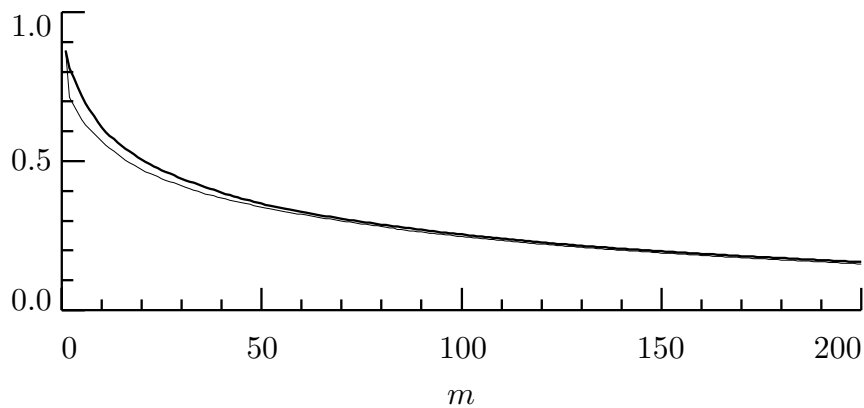


**Figure 248b.** Normalized residual sum of squares  $\|\mathbf{R}^{(m)}\|^2/\|\mathbf{X}\|^2$  versus the number of terms  $m$  in the matching pursuit approximation using the MODWT dictionary  $\mathbb{D}^{(\text{modwt})}$  (thick curve) and this dictionary combined with vectors from the ODFT (thin curve).